A&A, 690, A216 (2024)
https://doi.org/10.1051/0004-6361/202348572

Astronomy & Astrophysics

Varying linear polarisation in the dust-free gamma-ray burst 210610B

J. F. Agüí Fernández[1,⋆], A. de Ugarte Postigo[2,3], C. C. Thöne[4], S. Kobayashi[5], A. Rossi[6], K. Toma[7,8], M. Jelínek[4], D. A. Kann[1,9], S. Covino[10], K. Wiersema[11], D. Hartmann[12], P. Jakobsson[13], A. Martin-Carrillo[14], A. Melandri[15,10], M. De Pasquale[16], G. Pugliese[17], S. Savaglio[6,18,19], R. L. C. Starling[20], J. Štrobl[4], M. Della Valle[21], S. de Wet[22], and T. Zafar[23,24]

(Affiliations can be found after the references)

Received 12 November 2023 / Accepted 23 February 2024

ABSTRACT

Context. Long gamma-ray bursts (GRBs) are produced by the collapse of some very massive stars, that emit ultra-relativistic jets. When the jets collide with the interstellar medium they decelerate and generate the so-called afterglow emission, which has been observed to be polarised.
Aims. We study the polarimetric evolution of the GRB 210610B afterglow, at $z = 1.1341$. This allows us to evaluate the role of geometric and/or magnetic mechanisms in the GRB afterglow polarisation.
Methods. We observed GRB 210610B using imaging polarimetry with CAFOS on the 2.2 m Calar Alto Telescope and FORS2 on the 4×8.1 m Very Large Telescope. Complementary optical spectroscopy was obtained with OSIRIS on the 10.4 m Gran Telescopio Canarias. We studied the GRB light-curve from X-rays to the optical bands and the Spectral Energy Distribution (SED). This allowed us to strongly constrain the line-of-sight extinction. Finally, we studied the GRB host galaxy using optical to NIR data to fit the SED and derive its integrated properties.
Results. GRB 210610B had a bright afterglow with a negligible line-of-sight extinction. Polarimetry was obtained at three epochs: during an early plateau phase, at the time when the light curve breaks, and after the light curve steepened. We observe an initial polarisation of ∼4% that goes to zero at the time of the break, and it then again increases to ∼2%, with a change in the position angle of 54 ± 9 deg. The spectrum shows features with very low equivalent widths. This indicate a small amount of material in the line of sight within the host.
Conclusions. The lack of dust and the low amount of material in the line of sight to GRB 210610B allowed us to study the intrinsic polarisation of the GRB optical afterglow. The GRB polarisation signals are consistent with ordered magnetic fields in refreshed shock or/and hydrodynamics-scale turbulent fields in the forward shock.

Key words. polarization – techniques: polarimetric – gamma-ray burst: individual: GRB 210610B

1. Introduction

Gamma-ray bursts (GRBs) are among the most energetic electromagnetic explosions that have been observed in the Universe. These events have two main emission episodes: the prompt-emission and the afterglow-emission phases. The prompt emission represents the first observable electromagnetic emission and is dominated by gamma-ray photons lasting seconds to minutes after the onset of the burst. The afterglow has a synchrotron spectrum ranging from radio to gamma-rays and evolves in time during much longer time spans.

GRBs are typically classified as short or long according to their measured T_{90}[1] duration in gamma-rays (Kouveliotou et al. 1993). Short GRBs (sGRB) are associated with the coalescence of two compact objects, their T_{90} duration is typically shorter than 2 seconds, and their X-ray spectrum is hard. The discovery of a sGRB associated with the gravitational wave (GW) detection GW 170817 definitively linked a sGRB with the merger of two neutron stars (Abbott et al. 2017). On the other hand, long GRBs (lGRB) that show T_{90} longer than 2 seconds and have a softer spectra in the prompt emission phase. These are cataclysmic events associated with the collapse of massive stars. They are also associated with the detection of broad-line (BL) type Ic supernovae (SNe) (see e.g. Galama et al. 1998; Hjorth et al. 2003). Lately, several events detecting a kilonova (KN) emission in a burst with a duration of dozen seconds have cast doubts on the 2-seconds division as the unique criterion to distinguish between sGRBs and lGRBs (Rastinejad et al. 2022; Troja et al. 2022; Yang et al. 2022; Gompertz et al. 2023; Levan et al. 2023, 2024).

The prompt emission in a GRB is powered by a newly formed compact object that is fed by the surrounding material. Accretion onto this compact object launches ultra-relativistic jets, in which the prompt emission is generated through internal dissipation processes including internal shocks (see e.g. Rees & Meszaros 1994; Sari & Piran 1997; Kobayashi et al. 1997). This prompt high-energy emission releases isotropic-equivalent energies that can reach up to 10^{55} erg (see e.g. Burns et al. 2023), although the real released energy can be several orders of magnitude lower due to the jet collimation.

Polarimetry is an essential tool for explaining GRB physics. Using this technique, we can test models that include magnetic fields and the geometrical characteristics that are at play, and we can determine how they evolve throughout the different phases of the GRB. The study of the prompt emission polarisation and its temporal evolution can help us to understand how the jet is powered by the central engine. The long and extremely bright GRB 221009A was observed during the prompt- and afterglow-emission phase by the Imaging X-ray Polarimetry Explorer

⋆ Corresponding author; feli.agui.fernandez@gmail.com
[1] The T_{90} is the time span within which a GRB releases between 5% and 95% of the total energy during the prompt phase.

(IXPE) and only upper limits were obtained (Negro et al. 2023). Studies of the prompt-emission polarisation with instrument calibrated to perform polarimetry are rare so far. The Astrosat mission with the on-board Cadmium-Zinc-Telluride Imager (CZTI) instrument shows the prompt emission as highly polarised, while for POLAR, GRBs are lowly polarised or not polarised at all (see e.g. Gill et al. 2021).

The material ejected through the jets eventually collides with the circumburst material, decelerating as interacts with it. These forward shocks generate a broadband synchrotron emission that is known as the afterglow. This bright shock can be observed during days or even months in the case of radio frequencies. In certain cases, a reverse shock that propagates backwards within the relativistic jet can be observed at early times (see e.g. Mészáros & Rees 1997; Piran 1999). Different models predict this emission to be polarised. Gruzinov & Waxman (1999) proposed a model in which the afterglow would show patches with locally ordered magnetic fields randomly oriented but with many of them sharing a common direction leading to a global low level of polarisation in the GRB afterglow.

The number of studies using optical linear imaging polarimetry and spectropolarimetry techniques is still very small (see e.g. Covino & Gotz 2016). The first GRB with a polarisation detection in the afterglow was GRB 990510. Its polarisation degree (PD) was 1.7%, 0.7 days after detection (Covino et al. 1999; Wijers et al. 1999). Many efforts have been made to increase the sample of polarimetric measurements, but the faintness of these objects, their fast evolution, and the long observing times required for a good signal-to-noise ratio (S/N) leave us with less than 20 GRBs with a measurement above 3σ. Fast reaction is crucial for observing the first GRB phases in which a higher PD might be expected. The highest measured value was for GRB 120308A with a PD of 28% 5 minutes after the burst, which rapidly decreased to 16% as the afterglow evolved (Mundell et al. 2013). A high PD of ∼10% was also measured for GRB 020405, GRB 090102 and GRB 091208B (Bersier et al. 2003; Steele et al. 2009; Uehara et al. 2012). All of them were observed earlier than 0.01 days after the GRB detection. Observations at later stages shows this sources as lowly-polarised with some degree of variability throughout their light-curve evolution. The most detailed example is GRB 030329 (Greiner et al. 2003) whose PD evolves somewhat randomly from 0.91% at 0.5 days to 1.4% 37.5 days after the burst.

Afterglow polarisation must be understood together with the surrounding environment. Dust in the line of sight can change the observed PD and prevent the measurement of the intrinsic polarisation (Lazzati et al. 2003). This measurement by itself is also incomplete when it is not followed by the study of the light-curve evolution. It is crucial for distinguishing between the models that have been proposed to explain the GRB jet physics to understand whether there is a break in the light curve and how the polarisation behaves before, during and after this break (see e.g. Covino & Gotz 2016).

We present a comprehensive study of GRB 210610B, its afterglow emission and its environment using different techniques. Polarimetric, spectral and photometric observations were secured for this bright long GRB. We also observed the putative host galaxy in order to characterise it and place the GRB into context. This work is structured as follows: In Section 2 we present the observations of both, the afterglow and the underlying galaxy. In Section 3 we present the results of the analysis of the linear polarimetry of the afterglow, the light curve and its spectrum, as well as the analysis of the galaxy. In Section 4 we discuss the results by setting the framework into which GRB 210610B is embedded. We also place the results of the GRB afterglow polarimetry measurements into context. Finally, in Section 5 we present the conclusions.

Throughout this study, we describe the spectral and temporal evolution of the data using the convention by which $F_\nu \propto t^{-\alpha}\nu^{-\beta}$. We adopt a cosmological model with $H_0 = 67.3\,\mathrm{km\,s^{-1}\,Mpc^{-1}}$, $\Omega_\mathrm{M} = 0.315$ and $\Omega_\Lambda = 0.685$ (Planck Collaboration XVI 2014).

2. Observations

2.1. High-energy data

GRB 210610B was first detected by the Gamma-ray Burst Monitor (GBM) on board the *Fermi* observatory at 19:51:05.05 UT of 10 June 2021 with a $T_{90} = 55.04 \pm 0.72$ s and a fluence of $(1104.2 \pm 0.5) \times 10^{-5}\,\mathrm{erg\,cm^{-2}}$ in the 10 keV to 10 MeV band (Malacaria et al. 2021; von Kienlin et al. 2020). At the redshift of the GRB (see Sect. 3.3), the computed isotropic energy is $E_{\mathrm{iso,rest}} = 4.17^{+0.02}_{-0.02} \times 10^{53}$ erg in the 0.1 keV to 10 MeV band. This value is fully consistent with the so-called Amati relation (Amati et al. 2002; Amati 2006) for long GRBs. The burst was detected ∼22 s later by the Burst Alert Telescope (BAT; Barthelmy et al. 2005) on board the *Neil Gehrels Swift* Observatory with coordinates RA = $16^\mathrm{h}15^\mathrm{m}45^\mathrm{s}$, Dec = +14°23′29″ and an uncertainty of 3′. The X-Ray Telescope (XRT; Burrows et al. 2005) started observing the source 89.9 s after BAT and quasi-simultaneously, the Ultraviolet/Optical Telescope (UVOT; Roming et al. 2005) observed the field in the *White* band. The image showed a new bright source within the XRT position with a magnitude in the *Swift*/UVOT native system of 13.70 ± 0.14, uncorrected for galactic extinction (Page et al. 2021). The later analysis, presented in Siegel et al. (2021), updated this value to 13.63 ± 1.10 and the source location to RA = $16^\mathrm{h}15^\mathrm{m}40.40^\mathrm{s}$, Dec = +14°23′56.9″ with an uncertainty of 0.″42.

In the refined analysis from the BAT data, the burst had a T_{90} duration of $T_{90} = 69.38 \pm 2.53$ s in the 15 to 350 keV band with an $E_\mathrm{peak} = 339.3 \pm 218.6$ keV(Krimm et al. 2021). The burst showed a hardness ratio (HR)[2] of 1.78 ± 0.04. This falls in the upper part of the bulk of the HR distribution for long GRBs (see e.g. Lien et al. 2016). The burst was also detected by Konus-*Wind* observatory with a duration ∼100 s (Frederiks et al. 2021). The HR of the burst, its T_{90}, and its isotropic energy release classify GRB 210610B as a long GRB.

2.2. Linear polarimetry imaging

We observed the GRB 210610B following the *Swift*/BAT alert with two different instruments in linear polarimetry mode. We first observed it with the Calar Alto Faint Object Spectrograph (CAFOS) mounted on the 2.2 meter telescope at Calar Alto Observatory[3]. The observations started 0.08 days after the *Swift*/BAT detection with an exposure per half-wave plate (HWP) position angle (see below) of 900 s in *R* band. A second observation was obtained with the FOcal Reducer and low dispersion Spectrograph (FORS2) mounted on the Unit Telescope 1 of the Very Large Telescope (VLT) of the European Southern Observatory (ESO)[4]. The VLT/FORS2 observations started

[2] The hardness ratio or spectral hardness (Kouveliotou et al. 1993) for a GRB is the ratio between the fluence emitted during the prompt emission in the 50–100 keV band over the 25–50 keV band.

[3] Observations were obtained with programme F21-2.2-021 (PI: Agüí Fernández, J. F.).

[4] Observations were obtained with programme 106.21T6.003 (PI: Tanvir, N.).

0.24 days after the GRB alert in $R_{\rm Special}$, $b_{\rm High}$, and $z_{\rm Special}$ bands with 180 s exposure time per image and with two cycles with the same configuration.

For both instruments, observations were obtained using the HWP in four different rotation angles of 0.0°, 22.5°, 45.0°, and 67.5° and with a Wollaston prism to split the light into the ordinary (o) and extraordinary (e) beams. A mask was set to avoid overlapping of the light from the two beams.

To calibrate the CAHA/CAFOS observations, one high- and one zero-polarised standard star were observed following the same procedure as for the GRB. The flat-fields in the corresponding band were obtained with the full optical setup in the light path. For the VLT/FORS2 data, calibration and standard observations were performed as specified in the FORS2 User Manual (Anderson 2015).

We obtained a second epoch with VLT/FORS2 in $R_{\rm Special}$ ~ 1 day. We increased the exposure time per image up to 300 s to account for the fading of the source by performing two cycle for this observations.

2.3. Photometry

Photometric observations were performed using several instruments at different observatories and in multiple bands. In this section, we describe the details of each of the observations. The measured photometry is compiled in Table A.1.

2.3.1. Small Binocular Telescope

The Small Binocular Telescope (SBT), located at the Ondřejov Observatory, observed GRB 210610B at dusk with the two 20 cm Newtonian astrographs mounted on a common mount. The main detectors have 4096 × 4096 pixel CCDs that provide a field of view of 3.5° × 3.5° with a 3.14″ sampling. Operations are designed such that the readout time of one camera equals the exposure time of the other camera to avoid any blind time during the observation.

The SBT observations started ~860 s after the burst. During the early follow-up phase, 12 s exposures were taken without a filter. Afterwards, the observations consisted of up to 34 exposures of 120 s each in SDSS-r' band (see Table A.1 for further details). Observations were interrupted at 23:47 UT, almost 4 h after the GRB detection.

The afterglow was not detected in single exposures, and we therefore stacked the images to obtain an acceptable (S/N). We used `montage` to obtain a weighted image co-addition similarly to Morgan et al. (2008), which optimises for the variable background caused by dusk and thick cirrus.

As for the images in r' band, photometric calibration was performed against the Atlas catalogue, which uses the Pan-STARRS catalogue for faint targets. Images in the clear band were calibrated against the r' band and a polynomial correction involving photometric colours $g' - r'$, $r' - i'$, and $i' - z'$ was performed. Photometric measurements obtained this way are shifted compared to the original standard r' band by a correction that depends on the object colour. This correction can be computed from the fitted relation when the photometric colours of the afterglow are known. By fitting the complete photometric set with an empirical broken power law we, determined this correction to be $k_{c-r} = -0.0045$ mag. Therefore, under the assumption that the afterglow shows no colour evolution, we are able to convert the unfiltered values from SBT into r' by simply subtracting k_{c-r}.

2.3.2. FRAM-ORM telescope

The 25 cm telescope FRAM-ORM, is operated as part of CTA-N at Roque de los Muchachos at La Palma, Spain. The telescope is equipped with a 1024 × 1024 pixel CCD detector and a Bessel filter set, which provides a field of view of 26′ × 26′ with a pixel scale of 1.5″.

FRAM-ORM observed the GRB starting at 20:49 UT (1 h after trigger) and obtained a total of 83 × 60 s images in R band using a total of 1.5 h of observing time. Images were reduced using standard procedures and combined into groups in order to provide a good (S/N). Photometry was performed in a similar way as for the SBT unfiltered images, using r' band and $r' - i'$ band catalogue values. The derived correction factor is $k_{R-r} = -0.036$ mag.

2.3.3. Telescope D50

The D50 Telescope is a 0.5 m Newtonian robotic telescope located at Ondřejov Observatory. It has a 1024 × 1024 EMCCD camera with a field of view 20′ × 20′, scaled at 1.18″ per pixel. The telescope is equipped with an SDSS filter set.

D50 started observing 0.06 days after the burst detection, starting with SDSS-r' band and followed by a set of observations in SDSS-g', r', i', and z' bands using different exposure times (see Table A.1 for further details). During the first night, the telescope spent 3.2 h on target and stopped at 01:05 UT. There were additional observations in night 2, 4, 5, and 7, collecting 16.75 h of further follow-up data.

All images were processed in a standard manner performing dark subtraction, flat-field correction, and fringe removal for i' and z', and the images were co-added when necessary. Photometry was performed using the SDSS catalogue in the corresponding band. The GRB afterglow emission is detected even at the latest epoch.

2.3.4. CAHA/CAFOS

In addition to the polarimetric observation, we performed further imaging of the afterglow in the second night with CAFOS on the 2.2 m telescope of the Calar Alto Observatory. The images were corrected using bias and flat fields using standard procedures in IRAF. The observations were performed with the R_C filter and calibrated with respect to PanSTARRS field stars, for which a filter correction was used to derive AB magnitudes in the R_C band. These magnitudes were then transformed into the r' band using the colour information that we have from the afterglow. The final values are shown in Table A.1.

2.3.5. GTC/HiPERCAM

The field of GRB 210610B was observed in four epochs using the HiPERCAM multi-band imager (Dhillon et al. 2021) mounted on the 10.4 m Gran Telescopio de Canarias (GTC) at Roque de los Muchachos Observatory (La Palma, Spain) using programme GTCMULTIPLE2C-21A (PI: de Ugarte Postigo). HiPERCAM simultaneously obtains observations in the five SDSS filters (u', g', r', i', z') using efficient dichroic beam-splitters and multiple cameras. The last of our observations was obtained almost two months after the burst when the emission was dominated by the host galaxy (see Fig. 1).

The data reduction was performed using an automatic shell script that finds and organises the files, calls commands from the HiPERCAM pipeline to perform bias and flat corrections and

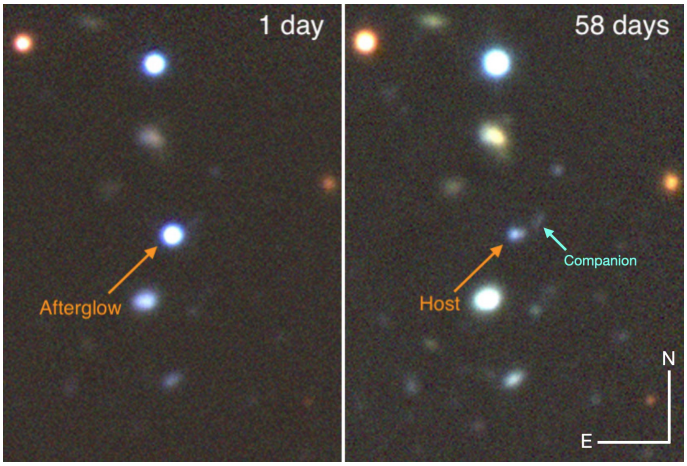

Fig. 1. Colour images of the field using the g', r' and i' bands of HiPERCAM at 1 day and 58 days after the burst, respectively. In the first image the afterglow is strongly detected, in the second image, it has faded and the host galaxy dominates the emission. 2.7 arcsec north-west of the host galaxy lies a companion galaxy at the same photometric redshift of the host (see Sect. 3.4).

converts the HiPERCAM one-dimension fits files into classical two-dimension fits images. Further IRAF procedures allow us to obtain an even background from the different quadrants of each detector. Finally, the images are registered and combined using SWARP (Bertin 2010). Photometry was performed with aperture photometry using reference field stars from the PanSTARRS catalogue. For the last epoch, we used the same aperture to compare the results to the rest of the data. Additionally, we performed photometry of the complete host galaxy adapting the aperture to its light, and in a similar way, we obtained photometry of a nearby object north-west of the host, which we identified as a companion galaxy at the same redshift (see Sect. 3.4).

2.3.6. Perek 2 m telescope

The Perek 2.0 m telescope at the Ondřejov Observatory observed GRB 210610B afterglow 6 days after the burst in SDSS-g' band. The photometric camera of this telescope has a 1092×736 pixel CCD with a field of view of $5' \times 7'$ scaled at $0.4''$/pixel. After standard imaging data reduction and after imaging co-addition, photometry was performed as for the D50 telescope. The GRB afterglow is well detected.

2.3.7. GTC/EMIR

Late-time near-infrared (NIR) observations were performed on 19 February 2022 in search for the host galaxy of GRB 210610B with the EMIR instrument (Garzón et al. 2022) mounted on the 10.4m GTC telescope with programme GTCMULTIPLE2H-21B (PI: de Ugarte Postigo). The observation consisted of a total exposure of 349×3 s in H band. The data reduction was performed using a self-made pipeline that corrects flat fields, does background subtraction, bad-pixel masking, alignment and combination of the frames. The host galaxy was not detected in the final frame down to a 3-σ limiting magnitude of 22.9 mag.

2.4. Spectroscopy

We observed GRB 210610B using the long-slit mode of the Optical System for Imaging and low Resolution Integrated Spectroscopy (OSIRIS) (Cepa et al. 2000) mounted on the 10.4 m GTC. The observation consisted of 3×900 s exposures with grism R1000B and a slit width of $1''$ oriented at the parallactic angle[5]. The mean epoch of the observation was 11 June 2021 at 01:59:14 UT (6.12972 h after the *Swift* trigger) at a mean airmass of 1.13.

Flux calibration was performed relative to an observation of the Ross 640 (Oke 1974) spectrophotometric standard, observed at the beginning of the same night and using the same grism. The afterglow spectrum shows a very strong continuum, with a median (S/N) of ~100 per dispersion element and weak absorption features.

3. Results

3.1. Linear polarimetric analysis

For all linear polarimetry data, we performed regular imaging-reduction processes. Images were bias subtracted and flat-field corrected using `PyRAF` tasks (Science Software Branch at STScI 2012). The flat field correction for VLT/FORS2 was performed as specified in González-Gaitán et al. (2020). For CAHA/CAFOS, we combined the flat fields using `PyRAF`, and we used a customized `Python` script to separate the o and e beams into two separate images. We normalised each beam to the corresponding median value and created the o and e beam combined flat. We followed the same procedure for each image. We performed this correction since flat fields were obtained with the full optics on the light pathway. This led to a rather different count rate in each beam what would have led to an inaccurate normalisation. Finally, we split all the reduced images into an o and e image and applied the `L.A. Cosmic` algorithm (van Dokkum 2001) to remove cosmic rays.

We used `PyRAF` to measure the on-frame full width at half maximum (FWHM) in each image including the high- and zero-polarised standard stars. The FWHM was measured independently for the o and e beam since the shape of the point spread function (PSF) can vary, especially for sources with a high degree of polarisation.

To obtain reference field stars we used a source detection algorithm based on `DAOStarFinder` in `Photutils` and applied it to the background-subtracted o and e images separately. The selected sources were those with a threshold above the median plus three times the standard deviation of the background. The statistics were calculated per beam and per angle position of the HWP using a sigma clipping of the masked image. From these sources, we discarded those that were clearly extended and those that lay too close or partially within the instrumental mask edges. We also checked whether the source was saturated in any of the beams. We ended up with five sources, including GRB 210610B, in the FORS2 images and five sources in the CAFOS images. The sources from FORS2 and CAFOS images are different due to saturation or because sources fall at the mask edges.

We performed aperture photometry using circular apertures with a radius equal to the FWHM and applied infinite-aperture corrections using a custom `Python` script to the FORS2 data. In order to avoid contamination by a nearby spurious source, we measured the flux for the CAHA/CAFOS data using a fixed aperture of three times the FWHM per image and per beam and subtracted the sky of an annulus around the source with an inner and outer radius of four and five times the FWHM, respectively. In the FORS2 images, this spurious source was outside the

[5] The observations were obtained under the program GTCMULTIPLE2C-21A (PI: de Ugarte Postigo).

measured region. The errors for the aperture photometry were obtained considering each beam as an unique image, that is, we separated the ordinary stripes from the extraordinary stripes.

With the measured flux values per source and per beam, f_o and f_e, we obtained the Stokes parameters Q and U describing the linear polarisation (see e.g. Patat & Romaniello 2006; Bagnulo et al. 2009) for each of our images. We used the normalised Stokes parameter for the linear polarisation.

$$\frac{Q}{I} = q = \frac{2}{N}\sum_{i=0}^{N-1} F_i \cos\frac{i\pi}{2} \tag{1}$$

$$\frac{U}{I} = u = \frac{2}{N}\sum_{i=0}^{N-1} F_i \sin\frac{i\pi}{2} \tag{2}$$

where N is the number of positions of the half-wave plate, I is the intensity, and F_i is the normalised flux difference per HWP position angle,

$$F_i = \frac{f_{\mathrm{o,i}} - f_{\mathrm{e,i}}}{f_{\mathrm{o,i}} + f_{\mathrm{e,i}}}. \tag{3}$$

Following the equations above, we can obtain the polarisation degree P_{lin},

$$P_{\mathrm{lin}} = \sqrt{q^2 + u^2}. \tag{4}$$

For the position angle, we followed the formalism as used in Bagnulo et al. (2009).

We then corrected for the effects of optics and detector in the polarisation images. To do this, zero-polarised standard stars were observed in the corresponding bands with VLT/FORS2 following the procedures detailed in Anderson (2015). For CAHA/CAFOS, observations of standard stars were carried out in the same night. In the case of VLT/FORS2, b- and z-band standards were completely saturated, and no subsequent standards were found in the ESO archive around the time of the observation. For the R band, the standards were also saturated. We then used WD1620−391 for the zero-polarised standard star, observed 18 days after the GRB, for VLT/FORS2, and BD+33 2642 (Turnshek et al. 1990) for CAHA/CAFOS observed in the same night as GRB 210610B.

We finally removed the effect on the polarisation induced by the dust in the Milky Way (MW). To do this, we measured the q and u parameters for the field stars in our images. However, FORS2 is known to have a radial profile in which the polarisation varies across the field from the optical axis towards the edges of the detectors (see e.g. González-Gaitán et al. 2020). To account for this effect, we applied the corresponding correction by using the q, u background correction and the instrumental polarisation maps presented in González-Gaitán et al. (2020). We then measured the Galactic interstellar polarisation (Galactic ISP, or GISP) using three methods, following Wiersema et al. (2012): First, we measured the mean values for the q, u parameters from the field stars. Then we performed a one-dimensional Gaussian fit to the q, u values of the field stars by generating a normal distribution of values for the q, u within their corresponding errors, and we then fitted a Gaussian to each Stokes parameter. Finally, we performed a two-dimensional Gaussian fit to the q, u, adapting the procedure from the one-dimensional Gaussian fit (see Fig. 2 for an example of the two-dimensional Gaussian fit). All the q, u fitted parameters are consistent within the errors, and we therefore vectorially subtracted the mean value from the q, u values for the GRB. The mean sky values are listed in Table 1,

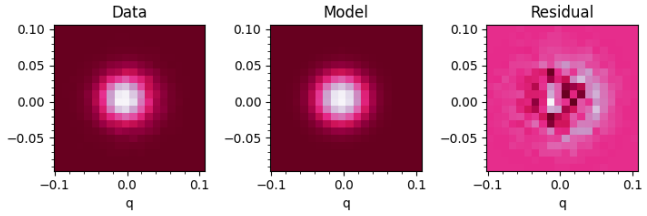

Fig. 2. Two-dimensional Gaussian fit to the field stars q, u parameters. Left: Normal distribution of randomly generated data around the q, u values. The amplitude to generate the data is the Stokes parameter errors. Central panel: two-dimensional Gaussian model fitted to the data points. Right: Residuals.

which are all consistent with or close to zero. Both q and u show some variation from one epoch to the next, which we assumed is due to different sky background light between the epochs[6].

For the CAFOS images, the same analysis was performed, although we were unable to correct for background polarisation and instrumental polarisation across the images because we lack a characterisation as we have for FORS2. However, lunar illumination was close to 0%, and we do not expect a high instrumental polarisation (Patat & Taubenberger 2011) for CAFOS. Indeed, the two-dimensional Gaussian fit to the field stars (see Fig. 2) shows it to be consistent with no polarisation from the ISM and implicitly, no polarisation from the CAFOS instrument.

After the polarisation induced by the MW dust was removed we calculated the final polarisation from both instruments in all the filters. Next, we needed to consider the contribution to the polarisation from the dust in the host galaxy itself. Since the information is more limited than for the dust in the MW we assumed a Serkowski law (Serkowski et al. 1975) for the host galaxy. From the spectral energy distribution (SED) fit of the GRB light curve, we obtained the colour excess on the line of sight (see Sect. 3.2). Assuming this value as the extinction of the afterglow at the host galaxy, using $P_{\mathrm{ISP}}(\%) \leq 9.0 \times E(B-V)$, we find that the contribution from the host galaxy could be as high as $P_{\mathrm{Host\,ISP}} \leq 0.09\%$. We note that in extragalactic sight lines, this may not be applicable because the dust properties may differ from those of the MW (Nagao et al. 2022). This value is well below the PD measured for the afterglow, and we therefore considered the host contribution to be negligible. Finally, we corrected for the polarisation definition bias with the modified asymptotic estimator (MAS) Plaszczynski et al. (2014). The corrected values for the polarisation degree are shown in Table 1 before and after the bias correction.

We also determined the polarisation position angle (PA) for the GRB afterglow. The FORS2-measured raw PA was corrected for chromaticity using the tabulated values per bandpass presented in Anderson (2015). We then corrected for it using the standard star Hiltner 652, observed on the 19, July 2021, although the PA correction is very small with $\Delta\theta = 0.5 \pm 0.9$. The high polarisation standard in R_{Special} band closest in time to the GRB was also saturated in at least one beam. We corrected the derived PA value of the standard to the value presented in Cikota et al. (2017). As the measured b-band value for the PA in Hiltner 652 is very close to the B band value in Cikota et al. (2017) we use B band to correct for the b-band value. For the z band, no observations were found so far for this standard, and we therefore used the PA for the I band in Cikota et al. (2017). The high polarisation standard observed for CAFOS, Hiltner 960,

[6] ESO weather log.

Table 1. Measured values for the linear polarisation and PA of GRB 210610B.

Epoch $t - t_0$ (day)	Bandpass	Instrument/Telescope	$q_{\rm sky}$ (%)	$u_{\rm sky}$ (%)	$P_{\rm Lin}$ (°)	$P_{\rm Lin,Debiased}$	θ	S/N
0.1205	R_C	CAHA/CAFOS	0.2 ± 2.4	-0.01 ± 0.31	4.50 ± 1.45	4.27 ± 1.45	183 ± 9	>500
0.2418	$R_{\rm Special}$	VLT/FORS2	-0.30 ± 0.32	-0.29 ± 0.20	0.28 ± 0.20	–	267 ± 19	>710
0.2593	$R_{\rm Special}$	VLT/FORS2	-0.79 ± 0.28	0.81 ± 0.22	0.60 ± 0.24	–	17 ± 11	>690
0.2698	$b_{\rm High}$	VLT/FORS2	–	–	0.18 ± 0.16	–	187 ± 24	>395
0.2803	$z_{\rm Special}$	VLT/FORS2	–	–	0.23 ± 0.28	–	199 ± 35	>180
1.2674	$R_{\rm Special}$	VLT/FORS2	-0.13 ± 0.22	0.06 ± 0.07	2.28 ± 0.22	2.27 ± 0.22	237 ± 3	>330
1.2766	$R_{\rm Special}$	VLT/FORS2	-0.36 ± 0.39	0.06 ± 0.07	1.72 ± 0.27	1.69 ± 0.27	238 ± 5	>300

Notes. When the standard corrected PA is negative, it was corrected to positive values by subtracting it from 360°. We measured the (S/N) in each beam and at each HWP angle image. The value we present here is the lowest we measured in one beam in one image at a certain HWP angle.

was corrected to the "theoretical" value following Schmidt et al. (1992).

We detect polarisation at $\gtrsim 3\sigma$ significance for the first and last epochs, while the second epoch is consistent with zero polarisation. We detect 1σ polarisation in the R band on the second epoch. We consider this measurement, together with the R band observation at ~0.26 days for the b and z band as limit, however. Since the MAS correction is not completely applicable when $\mathrm{PD}/\sigma_{\rm P} < 3.0$, we did not apply this correction to the mentioned limits. In this PD regime, the PA would behave erratically and, we therefore cannot treat it as a limit.

3.2. Light-curve analysis

We first modelled the optical and X-ray light curves simultaneously with a smoothly broken power law (Beuermann et al. 1999), $F = (F_1^{\kappa} + F_2^{\kappa})^{-1/\kappa}$, where $F_{\rm X} = f_{\rm break}(t/t_{\rm break})^{-\alpha_{\rm X}}$, $f_{\rm break}$ being the flux density at the break time $t_{\rm break}$, κ is the break smoothness parameter, and the subscripts 1, 2 indicate pre- and post-break, respectively. We did not consider data before 0.06 days (~5 ks) because they are still dominated by the initial rapid decay. Even before any modelling was performed, it is clear that the optical light curve is initially flat at least until ~0.25 days (~20 ks; see Fig. 3), while at the same time the X-ray behaviour is difficult to discern, though the two groups of observations at 4 ks and 7 ks show possible fading, in contrast to the optical. Not knowing the precise evolution of the early X-ray data, we allowed the initial X-ray decay to be different from the optical. Note that a different decay implies a colour evolution between X-rays and the optical. We find a shallow break with $t_{\rm break,\,opt} = 0.326 \pm 0.011$ d (27.7 ± 1.2 ks), a flat optical decay with $\alpha_{1,\rm opt} = 0.00 \pm 0.01$, and an optical to X-ray decay index $\alpha_{2,\rm break} = 1.85 \pm 0.04$, with a break smoothness $\kappa = 1.4 \pm 0.1$, with $\chi^2/\mathrm{d.o.f.} = 2.6$.

After the break, we analysed the full optical to X-ray SED when we the coverage in both frequency regimes was best. To build this SED, we first created the XRT spectra using the time-slice tool in the XRT repository (Evans et al. 2007, 2009) in the range 30 ks−50 ks at a mid-time of 1.2 days. We then shifted the optical GTC/HIPERCAM ugriz data at 1.097 days closer to these times using the decay indices found above.

We modelled the afterglow SED from optical to X-ray frequencies using `Xspec v12.13.0` (Arnaud 1996). The redshift was fixed to $z = 1.1341$, and we fixed the Galactic hydrogen column density to $N_{\rm H} = 3.94 \times 10^{20}\,\mathrm{cm}^{-2}$ (Willingale et al. 2013). The data are best modelled by a single power-law ($\chi^2/\mathrm{d.o.f.} = 264.5/298$) with $\beta = 0.869^{+0.003}_{-0.007}$, intrinsic absorption $N_{\rm H} = 18.3^{+6.5}_{-5.9} \times 10^{20}\,\mathrm{cm}^{-2}$ (using the Tübingen-Boulder ISM absorption model; Wilms et al. 2000) and $E(B-V) < 0.01$ mag, using the Small Magellanic Cloud (SMC) extinction law (Pei 1992).

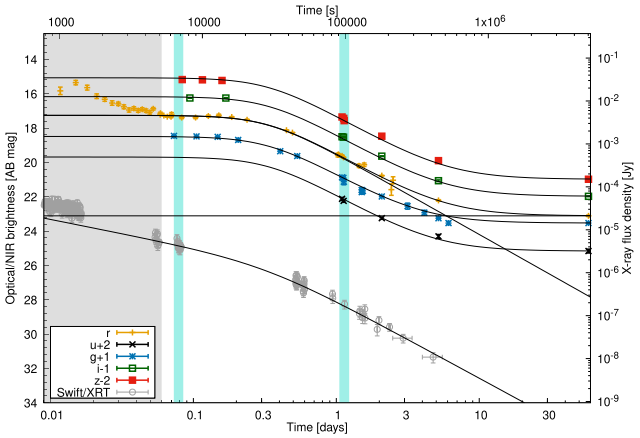

Fig. 3. GRB optical to X-ray light curve fit to available photometry (see Table A.1) and *Swift* X-ray data. The grey shaded region is not taken into account for the fit as it may be contaminated by the prompt emission. The clear cyan regions mark the times we chose to derive the SED of the light curve. The data are shown with an offset in flux for better visibility.

We also obtained an optical to X-ray SED at 0.079 days (6871 s) taking the X-ray data between 6000 and 8000 s and using the optical light curve above to shift the corresponding griz photometry. After fixing the redshift, extinction, and absorption as for the late epoch and following the same fitting procedure, we find that the data are best modelled by a broken power law ($\chi^2/\mathrm{d.o.f.} = 143.3/197$) with $\beta_{\rm opt} = 0.43^{+0.046}_{-0.046}$, and $\beta_{\rm X} = \beta_{\rm opt} + 0.5$, which indicates the presence of a spectral break, like the cooling break for synchrotron emission. We note that the spectral index of the high-frequency branch is consistent with the value found at late time, suggesting that the break shifted to lower frequencies with time, which is expected for an ISM environment within the fireball model and before the jet-break occurs (Sari et al. 1998). However, the shallow decay of the early light curve cannot be explained within the standard fireball model, unless we consider a more complex scenario such as an energy injection (e.g., Zhang et al. 2006).

3.3. Optical afterglow spectrum

The afterglow spectrum observed by OSIRIS ~0.25 days after the burst shows several transitions of Fe II, Mg II, and Mg I (see Table 2), all of them at a common redshift of $z = 1.1341 \pm 0.0004$

Table 2. Equivalent widths in the observer frame measured in the afterglow spectrum.

Observed λ (Å)	Feature	z'	EW (Å)
5001.69	Fe II 2344.21	1.1336	0.49 ± 0.07
5066.45	Fe II 2374.46	1.1337	0.23 ± 0.06
5084.79	Fe II 2382.77	1.1340	0.61 ± 0.07
5520.91	Fe II 2586.65	1.1344	0.25 ± 0.07
5549.64	Fe II 2600.17	1.1343	0.53 ± 0.07
5976.16	Mg II 2796.35	1.1341	3.29 ± 0.10
	Mg II 2803.53	1.1345	
6090.41	Mg I 2852.96	1.1348	0.64 ± 0.07
4353.92	Mg II 2796.35	0.5570	0.39 ± 0.10
4366.46	Mg II 2803.53	0.5575	0.23 ± 0.08

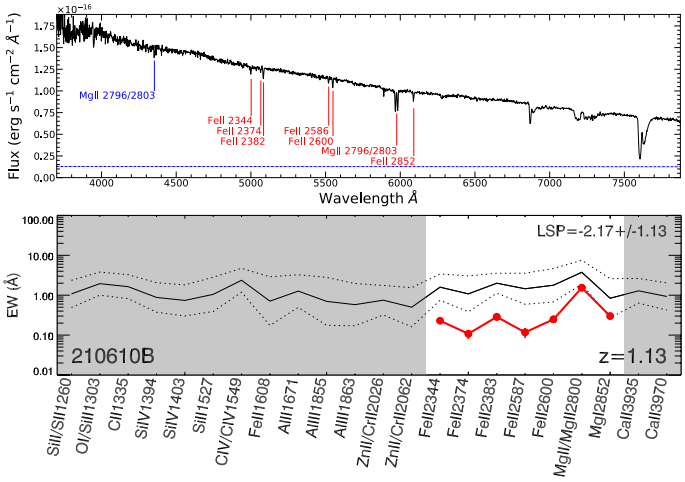

Fig. 4. Absorption spectroscopy and line properties for GRB 210610B. Top: Spectral features detected at the redshift of the GRB, plotted in red, and the features from the intervening system are shown in blue. The dashed blue line shows the error spectrum. Bottom: Line-strength diagram for the spectral features in the host galaxy. The diagram compares the features measured in our spectrum (red) with the average values of a larger sample (black) (see Sect. 3.3).

(see Fig. 4 and Table 2). This value is a lower limit for the burst redshift due to the non-detection of fine-structure lines excited by the GRB itself. The detection of the afterglow in the bluest band from *Swift*/UVOT sets an upper limit of $z = 1.7$, using the so-called Lyman drop-out technique, following (Jakobsson et al. 2012). Considering this limit and the lack of absorption lines common to GRBs (Christensen et al. 2011) at higher redshift, we hence adopted $z = 1.1341$ as the redshift of GRB 210610B. We also detected two absorption features that correspond to the Mg II doublet in an intervening system at $z = 0.5572 \pm 0.0002$.

The equivalent widths (EWs) of the detected absorption lines were measured using the GRBspec database tools (de Ugarte Postigo et al. 2014; Blažek et al. 2020) (see Table 2). We followed de Ugarte Postigo et al. (2012) to compare these values with the common trend for long GRB sight-line environments. The line strength parameter (LSP) measured for GRB 210610B is extremely low, $\mathrm{LSP} = -2.17 \pm 1.13$, implying that this line of sight has weaker features than 99.85% of the GRBs in the aforementioned sample. The line-strength diagram in Fig. 4 shows that the Fe II lines are particularly weak and are only detected through the very high signal-to-noise ratio of the spectrum. The magnesium features are stronger, but still among the weakest in the sample. The low EW values imply a low column density and hence a low amount of gas and possibly dust in the line of sight consistent with a negligible dust-induced polarisation.

3.4. Host galaxy

We observed the location of GRB 210610B ~58 days after the burst using GTC/HiPERCAM and ~253 days after with GTC/EMIR. In the HiPERCAM images, we detect an underlying object at the GRB position and we consider this object to be the host. We also find a putative companion galaxy towards north-west of the host candidate (see Fig. 1) at a distance of ~2.″7, which would correspond to a distance of 22 kpc at the redshift of the system. The photometry of the host galaxy is shown in Table A.1, together with the values for the companion.

We performed a SED analysis for the two galaxies assuming that both of them are at the GRB redshift. For this analysis, we used the SED fitting code `CIGALE`[7] (Burgarella et al. 2005; Noll et al. 2009; Boquien et al. 2019) in its latest version. To fit the star formation history (SFH), we chose a delayed star formation history with an age for the main stellar population ranging from 0.1 to 13 Gyr and a late burst with an age varying from 20−500 Myr. We allowed the code to vary the corresponding mass fraction from the total galaxy mass for the late burst from 0, which implies a single decaying exponential for the SFH modelling, up to 0.6, that is, 60% of the total galaxy mass. We use the initial mass function (IMF) as described in Chabrier (2003) with a Bruzual & Charlot (2003) stellar population model, assuming a stellar sub-solar metallicity (Z_*) for the galaxy (see Sects. 3.3 and 4) that was set to vary from 0.004 to 0.008, according to the scheme used in Bruzual & Charlot (2003). The nebular emission was modelled considering the same metallicity values for the gas.

For the attenuation law, we considered the modified Calzetti et al. (2000) law implemented in `CIGALE`, assuming a Small Magellanic Cloud (SMC) extinction law for the attenuation of the emission lines. We did not observe a colour evolution for the Galactic-dust-corrected (Schlafly & Finkbeiner 2011) magnitudes, and we do not detect the host galaxy in the *H* band down to 22.9 magnitudes. This might indicate a low level of dust emission due to low dust heating from UV massive star photons, indicating a low number of massive stars or an intrinsic lack of dust in this system. Since the amount of detected Mg, typically formed in the explosion of massive stars, is large compared to the amount of Fe in the traced system, although still low for common lGRBs sight-lines (see Fig. 4), this favours the scenario of low intrinsic extinction rather than the absence of massive stars (see Sect. 4 for an extended explanation). Therefore, we chose the colour excess of the nebular lines to be lower than 0.1. The slope of the attenuation curve (Boquien et al. 2019) was allowed to vary between −0.6 and 0.6. For the dust emission, we selected the Dale et al. (2014) models and allowed the exponent that controls the radiation field distribution of the re-emitted energy by dust heating to vary between 1.0 and 3.0.

We applied the same SED fit to both galaxies. However, the companion galaxy shows colour excess in the HiPERCAM observations, and we therefore allowed the colour excess for the nebular lines to range up to 0.4. The results for the com-

[7] https://cigale.lam.fr/

Table 3. Fitted physical properties of the putative host galaxy of GRB 210610B and its putative companion.

	Host galaxy	Host companion
$\log_{10}(M_*)\,(M_\odot)$	$9.10^{+0.40}_{-0.20}$	$9.60^{+0.55}_{-0.24}$
$\log_{10}(\mathrm{SFR})\,(M_\odot/\mathrm{yr})$	$1.06^{+0.12}_{-0.10}$	$0.47^{+0.32}_{-0.10}$
sSFR (Gyr^{-1})	9.26 ± 6.02	0.76 ± 0.68
A_V (mag)	0.19 ± 0.10	0.51 ± 0.33
Z_*	0.006 ± 0.002	0.006 ± 0.002
Reduced χ^2	0.49	0.50

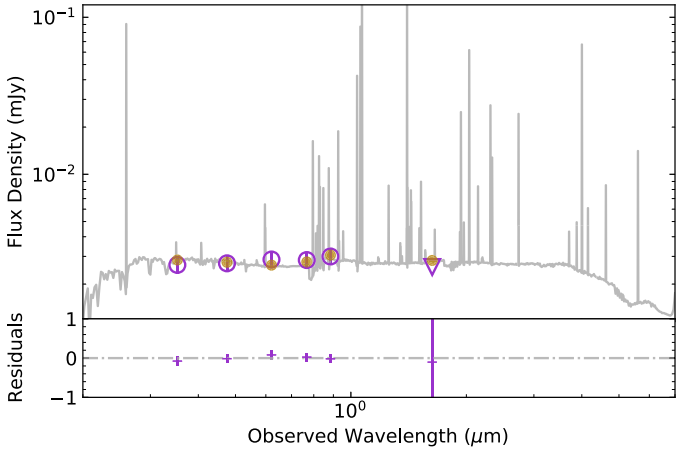

Fig. 5. GRB host SED with the corresponding residuals modelled using the CIGALE fitting code (Burgarella et al. 2005; Noll et al. 2009; Boquien et al. 2019) for the putative host galaxy of GRB 210610B. The vertical blue arrow indicates the *H* band upper limit.

puted physical properties from the SED fit can be found in Table 3 and the best fit is shown in Fig. 5. The SED of the companion galaxy allowed us to determine a photometric redshift that is consistent with the redshift for GRB 210610B. The companion is at a distance of 2.67 arcsec, corresponding to a physical distance of 22.6 kpc at a redshift of $z = 1.1341$. We therefore assumed that these two galaxies are part of a group.

4. Discussion

A broad study of the GRB prompt and afterglow emission together with its host galaxy is crucial for better constraints of the characteristics of GRB 210610B. The burst prompt emission presents the GRB as a hard burst, as observed by *Swift*, positioning it in the top part of the long GRB region of the hardness ratio versus T_{90} relation (see e.g. Lien et al. 2016). The isotropic equivalent energy, together with the observed peak energy, shows that GRB 210610B is fully consistent with the Amati relation (Amati et al. 2002; Amati 2006) for long GRBs. The prompt, high-energy emission of GRB 210610B has been analysed with Fermi data by Chen et al. (2022). They reported that the prompt emission is best fit by a hybrid jet model (Gao & Zhang 2015) in which a hot fireball component dominates the emission in the beginning, while a Poynting flux component supersedes at later times. Chen et al. (2022) described these results as consistent with the magnetar model as a plausible central engine (Metzger et al. 2011).

4.1. Host galaxy

The SED analysis of the GRB 210610B host reveals a galaxy with a low stellar mass, consistent with a dwarf galaxy that is actively forming stars and has low extinction. At the same redshift, the companion is more massive than the GRB host, with a higher stellar mass but lower SFR. The extinction for this galaxy is also higher than that of the GRB host assuming the same extinction law.

From the afterglow spectrum, we find that GRB 210610B is embedded in an environment with low amounts of Fe II and somewhat higher values for Mg II and Mg I. The low amount of Fe could be indicative of a low number of SN Ia in the host, since these explosions are the main sources of Fe (Pagel 2009). This could mean that either there is an intrinsic lack of this type of stellar explosions near the absorber site or that the system itself is too young to have been Fe-enriched via SN Ia. However, the absence of fine-structure lines in the spectrum does not allow us to determine the distance of the absorbing clouds to the explosion site and, therefore, the afterglow spectrum could be tracing gas in the external parts of the host galaxy, where we would expect it to be less enriched. Nevertheless, we find a higher relative value for the EWs of Mg, although it is still low compared to the mean value found for GRB sites (de Ugarte Postigo et al. 2012). Mg is released into the ISM through the explosion of massive stars (Pagel 2009). Together with the low amount of Fe, this might suggest that the host galaxy is a very young system. This is also supported by the extinction we measure from the SED fit. The A_V value may indicate that the host galaxy has a low amount of dust, which is expected for a low metallicity and, therefore, for a young system.

4.2. Afterglow

The GRB afterglow follows a decay-plateau-decay behaviour with an initial decay that is well fitted by a broken power law with an optical spectral slope at ~0.08 days of $\beta_{\mathrm{opt}} = 0.43^{+0.05}_{-0.05}$ and a $\beta_{\mathrm{XR}} \sim 0.83$. Afterwards, the light curve enters a plateau phase that lasts ~0.247 days to finally change to the final decay at ~0.326 days after burst. This final decay is better fitted by a power law with $\beta = 0.869^{+0.003}_{-0.007}$, consistent within errors with β_{XR} at ~0.08 days after GRB. The change in the spectral slope at ~0.08 days might be indicating a spectral break at the beginning of the plateau phase. The SED fit shows negligible extinction on the line of sight towards the GRB and a low X-ray hydrogen column density, as compared to N_{H} values for relatively low redshift GRBs (Campana et al. 2010). This low N_{H} together with the low $E(B-V)$, contradicts what would be expected for low-redshift bursts, where a higher dust-to-gas ratio is expected for lowly N_{H} X-ray absorbed bursts (Campana et al. 2010).

4.3. Polarisation

Our polarisation observations match three very important stages of the GRB 210610B afterglow light-curve. The first polarimetry measurements were performed 0.1205 days after burst, right after the light curve entered the plateau. The second epoch at ~0.26 days is close to the end of this plateau phase, almost consistent with the break of the optical light curve at 0.326 days after the GRB. After this, the light curve undergoes its final decay, where a final polarimetry epoch was observed. The afterglow is polarised at the beginning and towards the end of the light-curve evolution, but not around the optical break at 0.326 days after burst, where the polarisation drops to zero with a small rise to 0.61% in the next observation, which is slightly above the

$P_{\rm Host\,ISP}$ limit, but only at a 2.5-σ level. In the final decay, the polarisation increases to 2.27% and then decreases to 1.69% as the afterglow fades away. We find that b and z bands show polarisation values consistent with zero at a close epoch to the 2.5-σ R-band measurement. Therefore, the multi-band observations do not allow us to asses chromaticity/achromaticity in the afterglow polarisation. The PA varies by ∼54° between the 3σ detections. The measured polarisation is well consistent with prior measurements for linear polarimetry of GRB afterglows, as shown in Fig. 6.

One important aspect when determining the intrinsic polarisation is to constrain any contribution from the dust in the host galaxy. A possible polarisation from the MW was removed during the analysis (see Sect. 3.1). The SED fit to the GRB light curve results in a negligible value for the afterglow extinction on the line of sight and the inferred upper limit for the GRB host ISP is rather small compared to errors of the measured 3-σ polarisation detections (see Sect. 3.1). This means that either the polarisation contribution of the host galaxy along the line of sight is well below the $P_{\rm Host\,ISP}$ limit or that this contribution would cancel the afterglow polarisation out. The relatively high values we measured for the 3σ detections and the very low limit for the host galaxy polarisation led us to assume that the host contribution is negligible. This low extinction also supports the scenario in which the polarisation is interpreted as intrinsic to the GRB afterglow. This is further confirmed by the polarisation non-detection in the second epoch, which is an indirect measurement of the host ISP.

4.4. Theoretical Interpretations of the polarisation signals

The first polarimetry observations show a rather high linear polarisation degree of ∼4% at $t \sim 0.1205$ day. Considering that the observations were carried out during a shallow decay/plateau phase, a non-negligible fraction of optical photons might originate from refreshed shocks in the original ejecta from the central engine. As previous polarimetry studies of the early afterglow indicate that ejecta from the central engine contain large-scale ordered magnetic fields, at least for a subgroup of GRBs if not for all (e.g. Mundell et al. 2013), the refreshed shock emission can be polarised due to the ordered magnetic fields in the ejecta. The combination of the polarised refreshed shock emission and unpolarised forward shock emission is likely to give low-/intermediate-polarisation signals. For GRB 191016A, Shrestha et al. (2022) reported the detection of polarisation signals with $P \sim 5{-}15\%$ which are coincident with the start of the plateau phase. An energy injection model was discussed to explain the coincidence.

The optical light curve starts to decline at $t \sim 0.2$ days (see the top panel of Fig. 7). This indicates that the energy injection stops around that time and that the optical band is dominated by the forward-shock emission well before the second polarisation epoch is conducted at $t \sim 0.24$ day. The magnetic fields in the forward-shock region (the shocked ambient medium) are conventionally assumed to be generated locally by microscopic instabilities in shocks (see e.g. Medvedev & Loeb 1999), and they are expected to be highly tangled. The PD of the forward-shock emission is expected to be zero when the line of sight does not run along the jet edge. The low polarisation at $t \sim 0.24{-}0.28$ days can be explained naturally when the optical emission is dominated by the forward-shock emission.

Due to the relativistic beaming effect, the observer can see only a small visible region (a small patch with an angular size of $1/\Gamma$, located around the point at which the line of sight intersects the jet) instead of the entire surface of a shock front. The visible region appears as a ring due to a relativistic limb-brightening effect (Granot et al. 1999). Synchrotron emission from each small segment of the ring can be polarised when the random magnetic fields parallel and perpendicular to the shock normal have different averaged strengths. However, the net PD is zero because of the symmetry of the visible region.

As the forward shock slows down, the angular size of the visible region grows as $1/\Gamma \propto t^{3/8}$ (ISM) or $t^{1/4}$ (wind medium). Eventually, a part of the ring is located outside the jet edge and the emission region becomes asymmetric. This might have occurred by the third polarisation epoch at $t \sim 1.27$ day. Between the second and third epochs, the angular size of the visible region can grow by a factor of ∼1.7 (ISM) or 1.4 (wind medium). Optical linear polarisation measurements have been carried out for many late GRB afterglows typically several hours to a few days after the prompt gamma-ray emission (e.g. Covino & Gotz 2016). In this period, a jet break is expected to occur. The detection or upper limits of the linear PD are generally low (less than a few percent), which might indicate that the shock-generated random magnetic fields parallel and perpendicular to the shock normal have similar averaged strengths. The polarisation signals $P \sim 2\%$ at $t \sim 1.27$ days might be explained in this geometrical model. If the large-scale magnetic fields in the ejecta are toroidal, the PA change between $t \sim 0.24$ days and $t \sim 1.27$ days is expected to be 0 or 90°. However, the large-scale magnetic fields in the ejecta can be largely distorted before they inject energy into the forward shock (or the original magnetic structure can be very different from the toroidal configuration). The position angle change can be any value. However, this model predicts a steeper decline at late times. Even in the non-spreading jet model, the expected decay index is $\alpha = 3(p-1)/4 + 3/4 \sim 2.05$ (ISM) or $(3p-1)/4 + 1/2 \sim 2.30$ (wind medium) for $p = 2.74$, which is steeper than the observed value $\alpha = 1.85 \pm 0.04$. If we rely on the rather high value of p obtained from the SED modelling, we can rule this geometrical model out.

The nature of magnetic fields that are generated in shock instabilities is not yet fully understood. The microscopic-scale tangled magnetic fields may decay so rapidly in the downstream of the shock that they could not account for the observed synchrotron flux (e.g. Sironi et al. 2015). Alternatively, the forward-shock region could have magnetic field turbulence on large scales, comparable to the width of shocked region $\sim R/16\Gamma$ (e.g. Sironi & Goodman 2007). In this case, the PD and PA temporally change in a random manner, and PD $\sim 70\%/\sqrt{N}$, where N is the number of patches with a coherent magnetic field within the angular scale $1/\Gamma$ Gruzinov & Waxman (1999). Kuwata et al. (2023) constructed a semi-analytic model with a varying large-scale turbulent field in the forward-shock region, for which they performed numerical calculations in the case of isotropic turbulence and zero viewing angle. They obtained a randomly varying PD on a timescale of hours at a level of ∼1−3% and PA with changes that were not limited to 90°. These properties appear to be consistent with our data of GRB 210610B. When hydrodynamic-scale turbulent magnetic fields are assumed, we have two possible scenarios: (1) the ∼4%, ∼0.2%, and ∼2% polarisation signals are all due to turbulent magnetic fields, or (2) the ∼4% polarisation signal is due to polarised refreshed shock emission, and the other two signals are due to turbulent magnetic fields.

For non-spreading top-hat jets with microscopic-scale tangled fields, the PD light curve would have two maxima around a jet break, with the polarisation PA changing by 90° between the first and second maximum (Ghisellini & Lazzati 1999; Sari

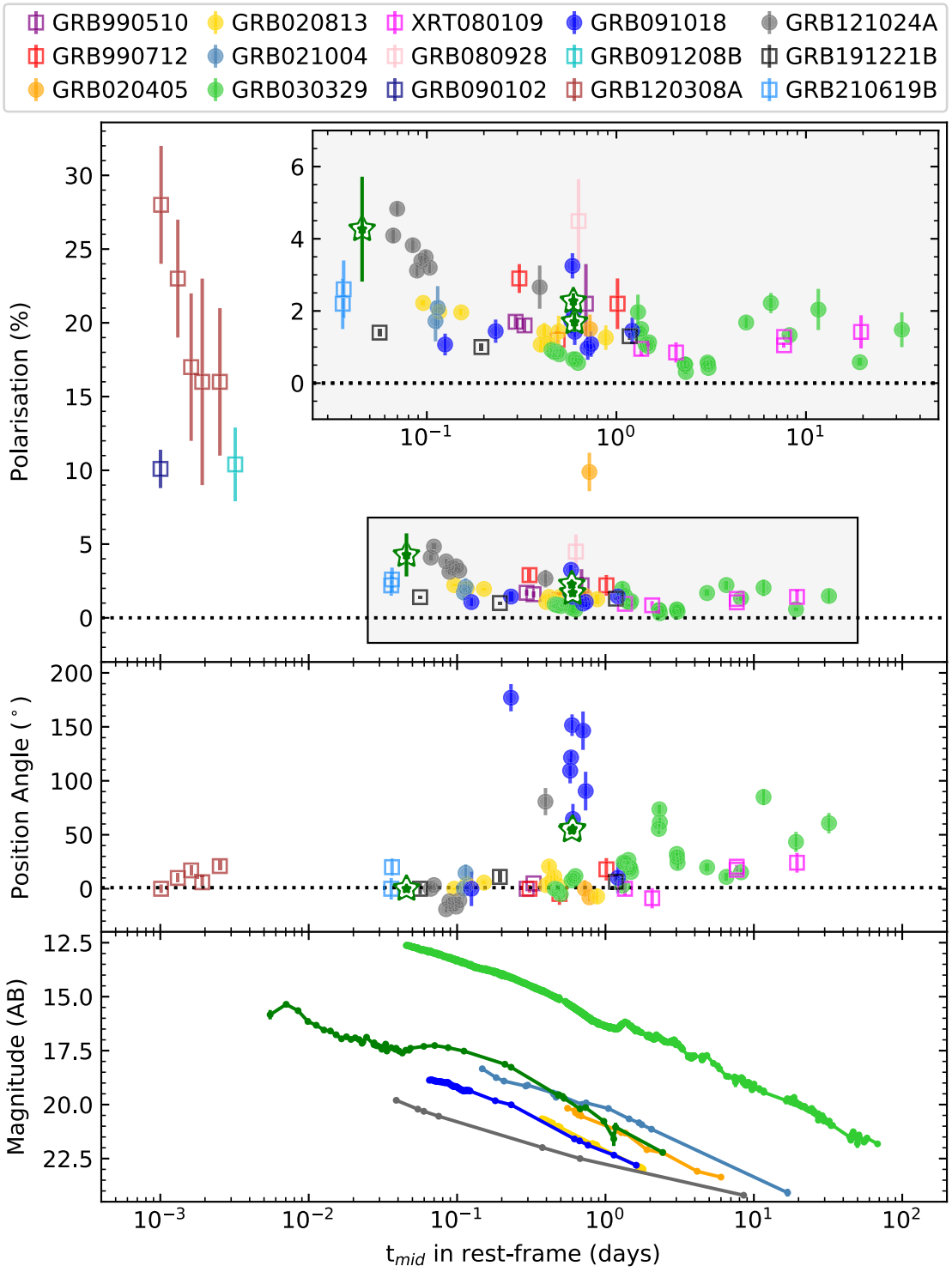

Fig. 6. Comparison of GRB 210610B polarisation evolution to previous detections of GRB afterglow positive polarisation. Top: Measured GRB linear polarisation degree on the optical afterglow emission. The white and green stars mark the polarisation degree measured for GRB 210610B in all bands. As for all the data points, we did not make a distinction on the photometric band in which the polarisation was measured. We only selected the measured values that show a $P/\sigma_P > 3$ for all bursts, including GRB 210610B. The filled circles indicate the bursts for which a light curve is shown in bottom panel, and empty squares represent the bursts that are not represented in this last panel. The data and references can be found in Table B.1. Middle panel: PA measured for each corresponding burst and epoch in the same fashion as in the top panel. Note that as for GRB 021004 there is no measured PA. To better distinguish the PA changes, we subtracted the first PA value to all values and calculated the absolute value for those with a mean value below zero. We do not find significant PA changes except for GRB 121024A, GRB 091018, GRB 030329, and GRB 210610B. We note that the measures were carried out with different instruments, and the data reduction and analysis can be different from the one we followed in this work. Bottom panel: Light curve for some exemplary burst with data available in the literature GRB 020405 (Masetti et al. 2003), GRB 020813 (Gorosabel et al. 2004), GRB 021004 (de Ugarte Postigo et al. 2005), GRB 030329 (Lipkin et al. 2004), GRB 091018 (Wiersema et al. 2012), GRB 121024A (Wiersema et al. 2014), and GRB 210610B.

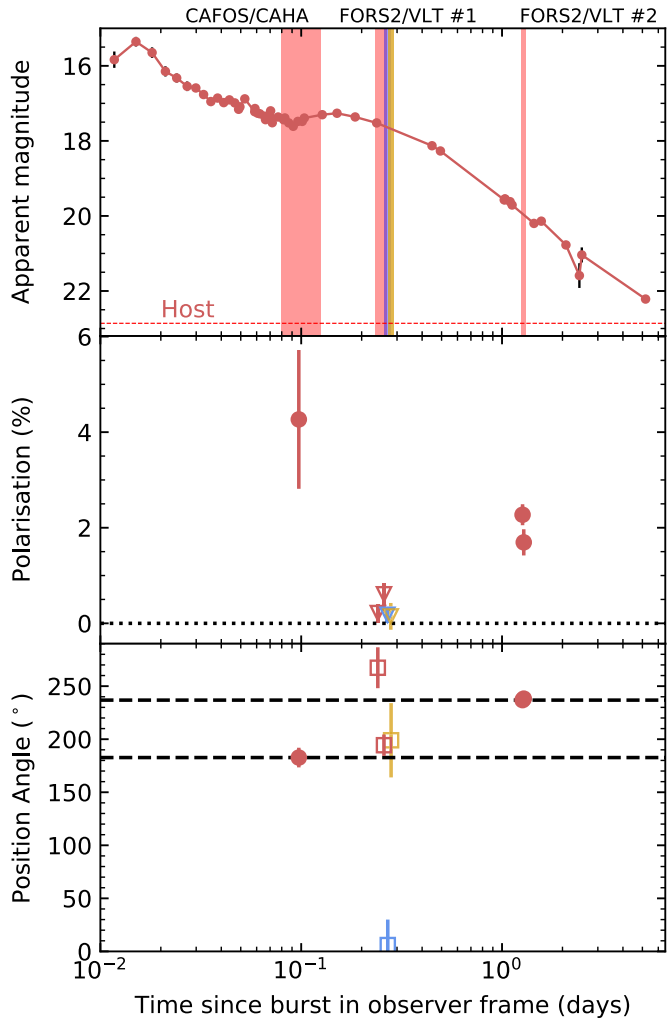

Fig. 7. Afterglow, PD and PA evolution of GRB 210610B. Top panel: GRB 210610B light curve for the r band (see Table A.1). We converted the SBT *Clear* band and R band into r band as indicated in Sects. 2.3.1 and 2.3.2. The vertical stripes from left to right denote the first polarimetry epoch (CAHA/CAFOS) and the second and third epochs (both with VLT/FORS2). The host observations in r band are marked with a dashed red line. Middle panel: Evolution of the linear polarisation of GRB 210610B. The red dots shows the measured polarisation for R band, and blue and orange triangles denote the lower limits in the b and z bands. Bottom panel: Linear polarisation measured PA for GRB 210610B. The detections are marked with filled circles, and the corresponding PAs for the PD limits are marked with empty squares as these values are neither lower nor upper limits. The dashed black lines denote the PA for the first (bottom) and the third (top) epoch.

1999). A possible jet break associated with the PA change of 90° has been detected for GRB 121024A (Wiersema et al. 2014). We studied a non-axisymmetric top-hat jet model (homogeneous jets with elliptic jet edge) to determine whether the main features can be explained in this model. Jets like this might be produced due to the interaction between jets and stellar envelope/neutron star wind ejecta (see Fig. 1 in Lamb et al. 2022) or jet precession (Huang et al. 2019). For non-axisymmetric jets, the PA change can be different from 90°. Following Sari (1999), we estimated the polarisation light curve and the PA change around a jet break. However, we find that this model does not work for this event. The main reasons are that (a) this model also predicts the steep decay at late times, as discussed in the geometrical model. (b) We needed to fine-tune the timing of the second polarisation measurement (we need to place the observation precisely in the "valley" of the polarisation curve), or equivalently, we needed to fine-tune a combination of parameters that provide the jet break time. (c) In the "valley", the polarisation needs to be very low (0.18−0.6%), compared to the earlier observation of ∼4%. To achieve this, Stokes u also needs to be almost zero when q flips sign. According to our rough parameter search (the geometrical parameters were ellipse eccentricity, ellipse orientation, and viewing angle), the eccentricity of the jet edge needs to be lower than roughly about 0.3. The low eccentricity does not allow the PA change to be significantly different from 90° (in our example case to fit the polarisation light curve, the PA change is about 80°).

5. Conclusions

GRB 210610B presents an exceptional scenario for performing polarimetry on the optical afterglow of a GRB. The light curve follows a decay-plateau-decay trend with a break after the plateau phase to a steep decay of the light curve. The SED modelling of the afterglow from X-rays to the optical indicates a dust free line of sight towards the GRB as well as a low $N_{\rm H}$. This negligible amount of dust is confirmed by the low A_V value we derive for the host galaxy and is further confirmed for the polarisation non-detection on the second polarimetry epoch. We also find that the GRB is embedded in a low-mass galaxy that seems to have a low amount of metals, which is indicative of a very young system.

The low amount of dust we find for GRB 210610B allowed us to study the intrinsic polarisation of the GRB afterglow. The optical afterglow is polarised at the beginning of the plateau phase of the light curve, disappears around the break achromatically, and reappears in the final decay of the light curve. In this complex behaviour, the first epoch seems to be dominated by the refreshed shock, which could explain the high polarisation value, while in the following epoch, the polarisation degree drops to zero as the forward shock would be dominating the optical emission. In the final decay of the light curve, the polarisation increases to ∼2% which could be explained assuming a geometrical model or hydrodinamics-scale turbulent magnetic fields.

Some models predict that GRB afterglow polarisation evolves from high polarisation at early stages, while the prompt emission or the refreshed shocks dominate, followed by a fast decay of the polarisation often reaching a zero polarisation. Afterwards, the polarisation again increases to moderate/low values, including changes in the polarisation position angle (see Covino & Gotz 2016 for a review). To better understand the polarisation evolution of GRBs, we should pursue two approaches: On one hand, we need to study polarisation throughout different GRB light curve phases, and on the other hand we need to obtain larger samples of GRBs.

Data availability

The CAFOS data are available at the CDS via anonymous ftp to cdsarc.cds.unistra.fr (130.79.128.5) or via https://cdsarc.cds.unistra.fr/viz-bin/cat/J/A+A/690/A216

Acknowledgements. JFAF acknowledges support from the Spanish Ministerio de Ciencia, Innovación y Universidades through the grant PRE2018-086507. JFAF acknowledges financial support from the Severo Ochoa grant CEX2021-001131-S funded by MCIN/AEI/10.13039/501100011033. AR acknowledge support from PRIN-MIUR 2017 (grant 20179ZF5KS). This work is partly based

on observations made with the Gran Telescopio Canarias (GTC), installed in the Spanish Observatorio del Roque de los Muchachos of the Instituto de Astrofísica de Canarias, in the island of La Palma. Partly based on observations collected at the Centro Astronómico Hispano en Andalucía (CAHA) at Calar Alto, operated jointly by Junta de Andalucía and Consejo Superior de Investigaciones Científicas (IAA-CSIC). This work made use of the GRBspec database https://grbspec.eu. This work has made extensive use of IRAF and Python, particularly with `astropy` (Astropy Collaboration 2013, http://www.astropy.org), `matplotlib` (Caswell et al. 2020), `photutils` (Bradley et al. 2019), `numpy` (Harris et al. 2020), and `Scipy` (Virtanen et al. 2020).

References

Abbott, B. P., Abbott, R., Abbott, T. D., et al. 2017, ApJ, 848, L13
Amati, L. 2006, MNRAS, 372, 233
Amati, L., Frontera, F., Tavani, M., et al. 2002, A&A, 390, 81
Anderson, J. 2015, FORS2 User Manual (European Southern Observatory), 96.0
Arnaud, K. A. 1996, ASP Conf. Ser., 101, 17
Astropy Collaboration (Robitaille, T. P., et al.) 2013, A&A, 558, A33
Bagnulo, S., Landolfi, M., Landstreet, J. D., et al. 2009, PASP, 121, 993
Barth, A. J., Sari, R., Cohen, M. H., et al. 2003, ApJ, 584, L47
Barthelmy, S. D., Barbier, L. M., Cummings, J. R., et al. 2005, Space Sci. Rev., 120, 143
Bersier, D., McLeod, B., Garnavich, P. M., et al. 2003, ApJ, 583, L63
Bertin, E. 2010, Astrophysics Source Code Library [record ascl:1010.068]
Beuermann, K., Hessman, F. V., Reinsch, K., et al. 1999, A&A, 352, L26
Blažek, M., de Ugarte Postigo, A., Kann, D. A., et al. 2020, SPIE Conf. Ser., 11452, 1145218
Boquien, M., Burgarella, D., Roehlly, Y., et al. 2019, A&A, 622, A103
Bradley, L., Sipőcz, B., Robitaille, T., et al. 2019, https://doi.org/10.5281/zenodo.3568287
Brivio, R., Covino, S., D'Avanzo, P., et al. 2022, A&A, 666, A179
Bruzual, G., & Charlot, S. 2003, MNRAS, 344, 1000
Burgarella, D., Buat, V., & Iglesias-Páramo, J. 2005, MNRAS, 360, 1413
Burns, E., Svinkin, D., Fenimore, E., et al. 2023, ApJ, 946, L31
Burrows, D. N., Hill, J. E., Nousek, J. A., et al. 2005, Space Sci. Rev., 120, 165
Calzetti, D., Armus, L., Bohlin, R. C., et al. 2000, ApJ, 533, 682
Campana, S., Thöne, C. C., de Ugarte Postigo, A., et al. 2010, MNRAS, 402, 2429
Caswell, T. A., Droettboom, M., Lee, A., et al. 2020, https://doi.org/10.5281/zenodo.3898017
Cepa, J., Aguiar, M., Escalera, V. G., et al. 2000, SPIE Conf. Ser., 4008, 623
Chabrier, G. 2003, PASP, 115, 763
Chen, J.-M., Peng, Z.-Y., Du, T.-T., & Yin, Y. 2022, ApJ, 932, 25
Christensen, L., Fynbo, J. P. U., Prochaska, J. X., et al. 2011, ApJ, 727, 73
Cikota, A., Patat, F., Cikota, S., & Faran, T. 2017, MNRAS, 464, 4146
Covino, S., & Gotz, D. 2016, Astron. Astrophys. Trans., 29, 205
Covino, S., Lazzati, D., Ghisellini, G., et al. 1999, A&A, 348, L1
Covino, S., Malesani, D., Ghisellini, G., et al. 2003, A&A, 400, L9
Dale, D. A., Helou, G., Magdis, G. E., et al. 2014, ApJ, 784, 83
de Ugarte Postigo, A., Castro-Tirado, A. J., Gorosabel, J., et al. 2005, A&A, 443, 841
de Ugarte Postigo, A., Fynbo, J. P. U., Thöne, C. C., et al. 2012, A&A, 548, A11
de Ugarte Postigo, A., Blazek, M., Janout, P., et al. 2014, SPIE Conf. Ser., 9152, 91520B
Dhillon, V. S., Bezawada, N., Black, M., et al. 2021, MNRAS, 507, 350
Evans, P. A., Beardmore, A. P., Page, K. L., et al. 2007, A&A, 469, 379
Evans, P. A., Beardmore, A. P., Page, K. L., et al. 2009, MNRAS, 397, 1177
Frederiks, D., Golenetskii, S., Lysenko, A., et al. 2021, GRB Coordinates Network, 30196, 1
Fynbo, J. P. U., Izzo, L., de Ugarte Postigo, A., Malesani, D. B., & Pursimo, T. 2021, GRB Coordinates Network, 30182, 1
Galama, T. J., Vreeswijk, P. M., van Paradijs, J., et al. 1998, Nature, 395, 670
Gao, H., & Zhang, B. 2015, ApJ, 801, 103
Garzón, F., Balcells, M., Gallego, J., et al. 2022, A&A, 667, A107
Ghisellini, G., & Lazzati, D. 1999, MNRAS, 309, L7
Gill, R., Kole, M., & Granot, J. 2021, Galaxies, 9, 82
Gompertz, B. P., Ravasio, M. E., Nicholl, M., et al. 2023, Nat. Astron., 7, 67
González-Gaitán, S., Mourão, A. M., Patat, F., et al. 2020, A&A, 634, A70
Gorosabel, J., Rol, E., Covino, S., et al. 2004, A&A, 422, 113
Gorosabel, J., de Ugarte Postigo, A., Castro-Tirado, A. J., et al. 2010, A&A, 522, A14
Granot, J., Piran, T., & Sari, R. 1999, ApJ, 513, 679
Greiner, J., Klose, S., Reinsch, K., et al. 2003, Nature, 426, 157
Gruzinov, A., & Waxman, E. 1999, ApJ, 511, 852
Harris, C. R., Millman, K. J., van der Walt, S. J., et al. 2020, Nature, 585, 357
Hjorth, J., Sollerman, J., Møller, P., et al. 2003, Nature, 423, 847
Ho, A. Y. Q., Perley, D. A., Yao, Y., et al. 2022, ApJ, 938, 85
Huang, B.-Q., Lin, D.-B., Liu, T., et al. 2019, MNRAS, 487, 3214
Jakobsson, P., Hjorth, J., Malesani, D., et al. 2012, ApJ, 752, 62
Kobayashi, S., Piran, T., & Sari, R. 1997, ApJ, 490, 92
Kouveliotou, C., Meegan, C. A., Fishman, G. J., et al. 1993, ApJ, 413, L101
Krimm, H. A., Barthelmy, S. D., Cummings, J. R., et al. 2021, GRB Coordinates Network, 30207, 1
Kuwata, A., Toma, K., Kimura, S. S., Tomita, S., & Shimoda, J. 2023, ApJ, 943, 118
Lamb, G. P., Nativi, L., Rosswog, S., et al. 2022, Universe, 8, 612
Lazzati, D., Covino, S., di Serego Alighieri, S., et al. 2003, A&A, 410, 823
Levan, A. J., Malesani, D. B., Gompertz, B. P., et al. 2023, Nat. Astron., 7, 976
Levan, A. J., Gompertz, B. P., Salafia, O. S., et al. 2024, Nature, 626, 737
Lien, A., Sakamoto, T., Barthelmy, S. D., et al. 2016, ApJ, 829, 7
Lipkin, Y. M., Ofek, E. O., Gal-Yam, A., et al. 2004, ApJ, 606, 381
Magalhaes, A. M., Pereyra, A., Dominici, T., & Abraham, Z. 2003, GRB Coordinates Network, 2163, 1
Malacaria, C., Hristov, B., & Fermi GBM Team 2021, GRB Coordinates Network, 30199, 1
Mandarakas, N., Blinov, D., Aguilera-Dena, D. R., et al. 2023, A&A, 670, A144
Masetti, N., Palazzi, E., Pian, E., et al. 2003, A&A, 404, 465
Medvedev, M. V., & Loeb, A. 1999, ApJ, 526, 697
Mészáros, P., & Rees, M. J. 1997, ApJ, 476, 232
Metzger, B. D., Giannios, D., Thompson, T. A., Bucciantini, N., & Quataert, E. 2011, MNRAS, 413, 2031
Morgan, A. N., Vanden Berk, D. E., Roming, P. W. A., et al. 2008, ApJ, 683, 913
Mundell, C. G., Kopač, D., Arnold, D. M., et al. 2013, Nature, 504, 119
Nagao, T., Patat, F., Maeda, K., et al. 2022, ApJ, 941, L4
Negro, M., Di Lalla, N., Omodei, N., et al. 2023, ApJ, 946, L21
Noll, S., Burgarella, D., Giovannoli, E., et al. 2009, A&A, 507, 1793
Oke, J. B. 1974, ApJS, 27, 21
Page, K. L., Gropp, J. D., Kennea, J. A., et al. 2021, GRB Coordinates Network, 30170, 1
Pagel, B. E. J. 2009, Nucleosynthesis and Chemical Evolution of Galaxies (Cambridge: Cambridge University Press)
Patat, F., & Romaniello, M. 2006, PASP, 118, 146
Patat, F., & Taubenberger, S. 2011, A&A, 529, A57
Pei, Y. C. 1992, ApJ, 395, 130
Perley, D. A. 2021, GRB Coordinates Network, 30216, 1
Piran, T. 1999, Phys. Rep., 314, 575
Planck Collaboration XVI. 2014, A&A, 571, A16
Plaszczynski, S., Montier, L., Levrier, F., & Tristram, M. 2014, MNRAS, 439, 4048
Rastinejad, J. C., Gompertz, B. P., Levan, A. J., et al. 2022, Nature, 612, 223
Rees, M. J., & Meszaros, P. 1994, ApJ, 430, L93
Rol, E., Wijers, R. A. M. J., Vreeswijk, P. M., et al. 2000, ApJ, 544, 707
Rol, E., Wijers, R. A. M. J., Fynbo, J. P. U., et al. 2003, A&A, 405, L23
Roming, P. W. A., Kennedy, T. E., Mason, K. O., et al. 2005, Space Sci. Rev., 120, 95
Sari, R. 1999, ApJ, 524, L43
Sari, R., & Piran, T. 1997, MNRAS, 287, 110
Sari, R., Piran, T., & Narayan, R. 1998, ApJ, 497, L17
Schlafly, E. F., & Finkbeiner, D. P. 2011, ApJ, 737, 103
Schmidt, G. D., Elston, R., & Lupie, O. L. 1992, AJ, 104, 1563
Science Software Branch at STScI 2012, Astrophysics Source Code Library [record ascl:1207.011]
Serkowski, K., Mathewson, D. S., & Ford, V. L. 1975, ApJ, 196, 261
Shrestha, M., Steele, I. A., Kobayashi, S., et al. 2022, MNRAS, 509, 5964
Siegel, M. H., Baer, M., Page, K. L., & Swift/UVOT Team 2021, GRB Coordinates Network, 30247, 1
Sironi, L., & Goodman, J. 2007, ApJ, 671, 1858
Sironi, L., Keshet, U., & Lemoine, M. 2015, Space Sci. Rev., 191, 519
Steele, I. A., Mundell, C. G., Smith, R. J., Kobayashi, S., & Guidorzi, C. 2009, Nature, 462, 767
Troja, E., Fryer, C. L., O'Connor, B., et al. 2022, Nature, 612, 228
Turnshek, D. A., Bohlin, R. C., Williamson, R. L., et al. 1990, AJ, 99, 1243
Uehara, T., Toma, K., Kawabata, K. S., et al. 2012, ApJ, 752, L6
Urata, Y., Toma, K., Covino, S., et al. 2023, Nat. Astron., 7, 80
van Dokkum, P. G. 2001, PASP, 113, 1420
Virtanen, P., Gommers, R., Oliphant, T. E., et al. 2020, Nat. Meth., 17, 261
von Kienlin, A., Meegan, C. A., Paciesas, W. S., et al. 2020, ApJ, 893, 46
Wiersema, K., Curran, P. A., Krühler, T., et al. 2012, MNRAS, 426, 2
Wiersema, K., Covino, S., Toma, K., et al. 2014, Nature, 509, 201
Wijers, R. A. M. J., Vreeswijk, P. M., Galama, T. J., et al. 1999, ApJ, 523, L33
Willingale, R., Starling, R. L. C., Beardmore, A. P., Tanvir, N. R., & O'Brien, P. T. 2013, MNRAS, 431, 394
Wilms, J., Allen, A., & McCray, R. 2000, ApJ, 542, 914
Yang, J., Ai, S., Zhang, B.-B., et al. 2022, Nature, 612, 232

Zhang, B., Fan, Y. Z., Dyks, J., et al. 2006, ApJ, 642, 354

[1] Instituto de Astrofísica de Andalucía, Glorieta de la Astronomía s/n, 18008 Granada, Spain
[2] Observatoire de la Côte d'Azur, Université Côte d'Azur, Boulevard de l'Observatoire, 06304 Nice, France
[3] Aix Marseille Univ., CNRS, CNES, LAM, Marseille, France
[4] Astronomical Institute of the Czech Academy of Sciences (ASU-CAS), Fričova 298, 251 65 Ondřejov, Czech Republic
[5] Astrophysics Research Institute, Liverpool John Moores University, 146 Brownlow Hill, Liverpool L3 5RF, UK
[6] INAF – Osservatorio di Astrofisica e Scienza dello Spazio, Via Piero Gobetti 93/3, 40129 Bologna, Italy
[7] Frontier Research Institute for Interdisciplinary Sciences, Tohoku University, Sendai 980-8578, Japan
[8] Astronomical Institute, Graduate School of Science, Tohoku University, Sendai 980-8578, Japan
[9] Hessian Research Cluster ELEMENTS, Giersch Science Center, Max-von-Laue-Strasse 12, Goethe University Frankfurt, Campus Riedberg, 60438 Frankfurt am Main, Germany
[10] INAF – Brera Astronomical Observatory, Merate, Italy
[11] Centre for Astrophysics Research, University of Hertfordshire, Hatfield AL10 9AB, UK
[12] Clemson University, Department of Physics and Astronomy, Clemson, SC 29634, USA
[13] Centre for Astrophysics and Cosmology, Science Institute, University of Iceland, Dunhagi 5, 107 Reykjavík, Iceland
[14] School of Physics and Centre for Space Research, O'Brien Centre for Science North, University College Dublin, Belfield, Dublin 4, Ireland
[15] INAF – Rome Astronomical Observatory, Via Frascati 33, I-00078 Monte Porzio Catone, Italy
[16] University of Messina, MIFT Department, Via F. S. D'Alcontres 31, 98166 Messina, Italy
[17] Astronomical Institute Anton Pannekoek, University of Amsterdam, PO Box 94249, 1090 GE Amsterdam, The Netherlands
[18] Physics Department, University of Calabria, Via P. Bucci, 87036 Arcavacata di Rende, CS, Italy
[19] INFN-Laboratori Nazionali di Frascati, Via Enrico Fermi 54, 00044 Frascati, RM, Italy
[20] School of Physics and Astronomy, University of Leicester, University Road, Leicester LE1 7RH, UK
[21] Capodimonte Astronomical Observatory, INAF-Napoli, Salita Moiariello 16, 80131 Napoli, Italy
[22] Inter-University Institute for Data Intensive Astronomy & Department of Astronomy, University of Cape Town, Private Bag X3, Rondebosch 7701, South Africa
[23] School of Mathematical and Physical Sciences, Macquarie University, Macquarie, NSW 2109, Australia
[24] ARC Centre of Excellence for All Sky Astrophysics in 3 Dimensions (ASTRO-3D), Australia

Appendix A: Afterglow and host galaxy photometry

Table A.1. Photometry of the afterglow of GRB 210610B.

Epoch t-t_0 (day)	Band	Telescope/ Instrument	Exposure (s)	Mag	Ref
1.09710	u'	GTC/HiPERCAM	10×60	20.311 ± 0.082	This Work
1.12521	u'	LT/IO:O	1×120	20.430 ± 0.082	[1]
2.08091	u'	GTC/HiPERCAM	10×60	21.438 ± 0.067	This Work
5.18532	u'	GTC/HiPERCAM	10×60	22.498 ± 0.112	This Work
58.1043	u'	GTC/HiPERCAM	30×60	23.353 ± 0.076	This Work
58.1043	u'	GTC/HiPERCAM	30×60	23.034 ± 0.076	This Work
58.1043	u'	GTC/HiPERCAM	30×60	24.901 ± 0.096	This Work
0.07316	g'	Ondrejov D50	3×300	17.597 ± 0.018	This work
0.10523	g'	Ondrejov D50	3×300	17.627 ± 0.019	This work
0.14793	g'	Ondrejov D50	3×300	17.652 ± 0.023	This work
0.20578	g'	Ondrejov D50	10×180	17.833 ± 0.083	This work
0.40536	g'	Palomar P48 Schmidt/ZTF	1×30	18.490 ± 0.020	[2]
0.53296	g'	Palomar P48 Schmidt/ZTF	1×30	18.770 ± 0.030	[2]
1.09710	g'	GTC/HiPERCAM	10×60	20.010 ± 0.040	This work
1.12103	g'	LT/IO:O	1×90	20.040 ± 0.050	[1]
1.12951	g'	Ondrejov D50	86×180	20.263 ± 0.181	This work
1.50546	g'	Palomar P48 Schmidt/ZTF	1×30	20.750 ± 0.140	[2]
1.50646	g'	Palomar P48 Schmidt/ZTF	1×30	20.870 ± 0.120	[2]
1.53416	g'	Palomar P48 Schmidt/ZTF	1×30	20.800 ± 0.140	[2]
2.08091	g'	GTC/HiPERCAM	10×60	21.124 ± 0.031	This work
3.15081	g'	Ondrejov D50	97×180	21.689 ± 0.177	This work
4.13012	g'	Ondrejov D50	78×180	22.067 ± 0.098	This work
5.18532	g'	GTC/HiPERCAM	10×60	22.394 ± 0.058	This work
6.09497	g'	Perek 2.0m	9×300	22.672 ± 0.098	This work
58.1043	g'	GTC/HiPERCAM	30×60	23.307 ± 0.043	This work
58.1043	g'	GTC/HiPERCAM	30×60	22.960 ± 0.044	This work
58.1043	g'	GTC/HiPERCAM	30×60	24.866 ± 0.053	This work
0.04880	R	FRAM-ORM	23×60	17.211 ± 0.065	This work
0.05869	r'	Ondrejov D50	1×300	17.322 ± 0.017	This work
0.06069	R	FRAM-ORM	8×60	17.314 ± 0.080	This work
0.06219	r'	Ondrejov D50	1×300	17.377 ± 0.014	This work
0.06568	r'	Ondrejov D50	1×300	17.441 ± 0.019	This work
0.06642	R	FRAM-ORM	7×60	17.487 ± 0.087	This work
0.06981	r'	Ondrejov SBT	17×120	17.442 ± 0.063	This work
0.07042	r'	NOT	1×10	17.299 ± 0.100	[3]
0.07176	R	FRAM-ORM	7×60	17.569 ± 0.087	This work
0.07673	R	FRAM-ORM	6×60	17.416 ± 0.079	This work
0.08170	R	FRAM-ORM	7×60	17.489 ± 0.078	This work
0.08290	r'	Ondrejov SBT	18×120	17.489 ± 0.066	This work
0.08667	R	FRAM-ORM	6×60	17.572 ± 0.096	This work
0.09125	R	FRAM-ORM	6×60	17.664 ± 0.097	This work
0.09621	R	FRAM-ORM	7×60	17.534 ± 0.084	This work
0.10119	R	FRAM-ORM	6×60	17.533 ± 0.095	This work
0.10362	r'	Ondrejov SBT	23×120	17.491 ± 0.063	This work
0.12734	r'	Ondrejov SBT	25×120	17.402 ± 0.058	This work
0.15077	r'	Ondrejov SBT	34×120	17.363 ± 0.071	This work
0.18566	r'	Ondrejov D50	10×180	17.462 ± 0.031	This work
0.23746	r'	GTC/OSIRIS	1×30	17.621 ± 0.040	This work
0.44806	r'	Palomar P48 Schmidt/ZTF	1×30	18.229 ± 0.020	[2]
0.49346	r'	Palomar P48 Schmidt/ZTF	1×30	18.369 ± 0.020	[2]
1.02539	r'	CAHA/CAFOS	1×60	19.672 ± 0.112	This work
1.03206	r'	CAHA/CAFOS	1×180	19.653 ± 0.035	This work
1.03495	r'	CAHA/CAFOS	1×180	19.647 ± 0.030	This work
1.03791	r'	CAHA/CAFOS	1×180	19.663 ± 0.027	This work
1.09710	r'	GTC/HiPERCAM	10×60	19.720 ± 0.050	This work
1.12244	r'	LT/IO:O	1×90	19.809 ± 0.020	[1]
1.44226	r'	Palomar P48 Schmidt/ZTF	1×30	20.299 ± 0.100	[2]
1.56876	r'	Palomar P48 Schmidt/ZTF	1×30	20.239 ± 0.100	[2]
2.08091	r'	GTC/HiPERCAM	10×60	20.873 ± 0.018	This work
2.42766	r'	Palomar P48 Schmidt/ZTF	1×30	21.689 ± 0.330	[2]
2.49606	r'	Palomar P48 Schmidt/ZTF	1×30	21.139 ± 0.200	[2]
5.18532	r'	GTC/HiPERCAM	10×60	22.315 ± 0.042	This work
58.1043	r'	GTC/HiPERCAM	30×60	23.212 ± 0.042	This work
58.1043	r'	GTC/HiPERCAM	30×60	22.861 ± 0.042	This work
58.1043	r'	GTC/HiPERCAM	30×60	24.486 ± 0.058	This work

Table A.1. continued.

Epoch t-t_0 (day)	Band	Telescope/ Instrument	Exposure (s)	Mag	Ref
0.09453	i'	Ondrejov D50	5×180	17.328 ± 0.016	This work
0.16882	i'	Ondrejov D50	5×180	17.330 ± 0.025	This work
1.09710	i'	GTC/HiPERCAM	10×60	19.585 ± 0.048	This work
1.12383	i'	LT/IO:O	1×90	19.609 ± 0.030	[1]
2.08091	i'	GTC/HiPERCAM	10×60	20.715 ± 0.022	This work
5.18532	i'	GTC/HiPERCAM	10×60	22.145 ± 0.047	This work
6.13124	i'	Ondrejov D50	96×180	> 22.760	This work
58.1043	i'	GTC/HiPERCAM	30×60	23.052 ± 0.023	This work
58.1043	i'	GTC/HiPERCAM	30×60	22.843 ± 0.024	This work
58.1043	i'	GTC/HiPERCAM	30×60	24.142 ± 0.049	This work
0.08363	z'	Ondrejov D50	5×180	17.234 ± 0.029	This work
0.11569	z'	Ondrejov D50	5×180	17.246 ± 0.028	This work
0.15862	z'	Ondrejov D50	5×180	17.285 ± 0.034	This work
1.0971	z'	GTC/HiPERCAM	10×60	19.413 ± 0.040	This work
1.1269	z'	LT/IO:O	1×90	19.491 ± 0.060	[1]
1.1354	z'	Ondrejov D50	9×300	19.624 ± 0.140	This work
2.0809	z'	GTC/HiPERCAM	10×60	20.530 ± 0.027	This work
5.1853	z'	GTC/HiPERCAM	10×60	21.953 ± 0.052	This work
58.1043	z'	GTC/HiPERCAM	30×60	23.037 ± 0.028	This work
58.1043	z'	GTC/HiPERCAM	30×60	22.769 ± 0.031	This work
58.1043	z'	GTC/HiPERCAM	30×60	23.620 ± 0.057	This work
0.01173	Clear	Ondrejov SBT	20×12	15.931 ± 0.218	This work
0.01504	Clear	Ondrejov SBT	20×12	15.451 ± 0.128	This work
0.01809	Clear	Ondrejov SBT	20×12	15.743 ± 0.141	This work
0.02108	Clear	Ondrejov SBT	20×12	16.243 ± 0.136	This work
0.02399	Clear	Ondrejov SBT	20×12	16.419 ± 0.120	This work
0.02705	Clear	Ondrejov SBT	20×12	16.640 ± 0.128	This work
0.02988	Clear	Ondrejov SBT	20×12	16.685 ± 0.099	This work
0.03266	Clear	Ondrejov SBT	20×12	16.860 ± 0.113	This work
0.03550	Clear	Ondrejov SBT	20×12	17.047 ± 0.119	This work
0.03835	Clear	Ondrejov SBT	20×12	16.954 ± 0.095	This work
0.04113	Clear	Ondrejov SBT	20×12	17.075 ± 0.099	This work
0.04391	Clear	Ondrejov SBT	20×12	17.002 ± 0.088	This work
0.04668	Clear	Ondrejov SBT	20×12	17.083 ± 0.096	This work
0.04953	Clear	Ondrejov SBT	20×12	17.187 ± 0.096	This work
0.05238	Clear	Ondrejov SBT	20×12	16.975 ± 0.075	This work
0.05886	Clear	Ondrejov SBT	43×12	17.233 ± 0.059	This work
252.3749	H	GTC/EMIR	349	> 22.9	This work

Notes. The magnitudes are given in the AB system and are not corrected for Galactic extinction. We give three magnitudes at 58 days, for the host galaxy measured in an aperture identical to that used in afterglow photometry, for the full host galaxy, and for the companion galaxy, respectively. The initial time is t_0 = 19:51:05.05 UT. Data from literature are: [1] (Perley 2021), [2] Ho et al. (2022) and [3] (Fynbo et al. 2021)

Appendix B: Linear polarisation measurements on GRBs afterglow emission.

Table B.1. Measured values for the linear polarisation and PA of GRB afterglows from the literature.

GRB	Redshift	T_{mid} (days)	P_{Lin} (%)	θ (°)	Ref
GRB 990510	1.62	0.7708	1.7 ± 0.2	101 ± 3	[1]
		0.8583	1.6 ± 0.2	96 ± 4	[2]
		1.8083	$2.2^{+1.1}_{-0.9}$	112^{+15}_{-17}	"
GRB 990712	0.43	0.44	2.9 ± 0.4	121.1 ± 3.5	[3]
		0.70	1.2 ± 0.4	116.2 ± 10.1	[3]
		1.45	2.2 ± 0.7	139.1 ± 10.4	"
GRB 020405	0.695	1.2292	1.50 ± 0.40	172 ± 8	[4]
		1.3208	9.89 ± 1.30	180 ± 4	[5]
		2.2682	1.96 ± 0.33	154 ± 5	[6]
		3.8792	1.47 ± 0.43	168 ± 9	"
GRB 020813	1.35	0.21528	2.22 ± 0.07	157.6 ± 1.0	[7]*
		0.26181	1.98 ± 0.04	153.4 ± 1.7	"
		0.34167	1.96 ± 0.07	152.0 ± 1.2	"
		0.89792	1.07 ± 0.22	154.3 ± 5.9	[8]
		0.93750	1.42 ± 0.25	137.0 ± 4.4	"
		0.97542	1.11 ± 0.22	150.5 ± 5.5	"
		1.01625	1.05 ± 0.23	146.4 ± 6.2	"
		1.11667	1.43 ± 0.44	155.8 ± 8.5	"
		1.97958	1.26 ± 0.34	164.7 ± 7.4	"
GRB 021004	2.33	0.37	1.72 ± 0.56	187.7 ± 8.3	[9]
		0.38	2.09 ± 0.60	173.0 ± 7.9	"
GRB 030329	0.17	0.5321	0.92 ± 0.10	86.13 ± 2.43	[10]**
		0.5492	0.86 ± 0.09	86.74 ± 2.40	"
		0.5671	0.87 ± 0.09	88.60 ± 2.64	"
		0.5850	0.80 ± 0.09	91.12 ± 2.88	"
		0.6921	0.66 ± 0.07	78.52 ± 2.94	"
		0.7129	0.66 ± 0.07	76.69 ± 2.89	"
		0.7342	0.56 ± 0.05	74.37 ± 3.11	"
		1.5204	1.97 ± 0.48	83.20	"
		1.5500	1.37 ± 0.11	61.65 ± 2.38	"
		1.5800	1.50 ± 0.12	62.29 ± 2.44	"
		1.6700	1.07 ± 0.09	59.41 ± 2.51	"
		1.7000	1.09 ± 0.08	66.07 ± 2.45	"
		1.7200	1.02 ± 0.08	67.05 ± 2.60	"
		1.7400	1.13 ± 0.08	70.56 ± 2.51	"
		2.6800	0.52 ± 0.06	30.76 ± 5.04	"
		2.7000	0.52 ± 0.12	12.55 ± 4.63	"
		2.7200	0.31 ± 0.07	24.50 ± 6.94	"

Table B.1. continued.

GRB	Redshift	T_{mid} (days)	P_{Lin} (%)	θ (°)	Ref
		3.5400	0.57 ± 0.09	53.85 ± 4.08	"
		3.5600	0.53 ± 0.08	57.08 ± 4.06	"
		3.5800	0.42 ± 0.10	62.21 ± 6.10	"
		5.6600	1.68 ± 0.18	66.32 ± 3.38	"
		7.6400	2.22 ± 0.28	75.16 ± 3.32	"
		9.5900	1.33 ± 0.14	70.91 ± 3.31	"
		13.6000	2.04 ± 0.57	1.16 ± 7.64	"
		22.5000	0.58 ± 0.10	42.7 ± 9.26	"
		37.5000	1.48 ± 0.48	25.42 ± 9.41	"
XR 080109	0.007	3.6416	0.95 ± 0.20	114.9 ± 5.9	[11]
		5.5552	0.85 ± 0.28	106.1 ± 9.4	"
		20.6279	1.05 ± 0.06	135.3 ± 1.7	"
		20.6443	1.28 ± 0.06	132.5 ± 1.4	"
		52.5578	1.42 ± 0.46	139.0 ± 9.1	"
GRB 080928	1.6919	1.7	$4.49^{+1.16}_{-0.96}$	41.3 ± 6.3	[12]
GRB 090102	1.55	0.0025	10.1 ± 1.3	–	[13]
GRB 091208B	1.063	0.0042	10.4 ± 2.5	92 ± 6	[14]
GRB 091018	0.971	0.2461	1.07 ± 0.30	179.2 ± 16.1	[15]
		0.4548	1.44 ± 0.32	2.2 ± 12.6	"
		1.1394	1.73 ± 0.36	69.8 ± 11.7	"
		1.1552	3.25 ± 0.35	57.6 ± 6.1	"
		1.1735	1.99 ± 0.35	27.6 ± 10.0	"
		1.1893	1.42 ± 0.36	114.6 ± 14.0	"
		1.3918	0.97 ± 0.32	32.8 ± 17.8	"
		1.4493	1.08 ± 0.35	88.7 ± 17.9	"
		2.3902	1.45 ± 0.37	169.0 ± 14.3	"
GRB 120308	2.22	0.0033	28^{+4}_{-4}	34 ± 4	[16]
		0.0042	23^{+4}_{-4}	44 ± 6	"
		0.0052	17^{+5}_{-4}	51 ± 9	"
		0.0062	16^{+7}_{-4}	40 ± 10	"
		0.0081	16^{+5}_{-4}	55 ± 9	"
GRB 121024A	2.298	0.2194	4.09 ± 0.2	163.7 ± 2.8	[17]
		0.2302	4.83 ± 0.2	160.3 ± 2.3	"
		0.2782	3.82 ± 0.2	182.7 ± 3.0	"
		0.2928	3.12 ± 0.19	175.3 ± 3.5	"
		0.3088	3.39 ± 0.18	178.0 ± 2.9	"
		0.3252	3.49 ± 0.18	180.3 ± 3.0	"
		0.3412	3.2 ± 0.18	174.5 ± 3.3	"
		1.2995	2.66 ± 0.6	83.0 ± 12.6	"
GRB 191221B	1.148	0.121	1.4 ± 0.1	68 ± 5	[18]
		0.417	1.0 ± 0.1	57 ± 5	"
		2.525	1.3 ± 0.1	62 ± 6	"
GRB 210610B	1.1345	0.0973	4.27 ± 1.45	183 ± 9	This work
		0.2407	0.22 ± 0.20	267 ± 19	"
		0.2688	0.03 ± 0.17	–	"
		0.2793	0.15 ± 0.28	–	"
		1.2655	2.27 ± 0.22	237 ± 3	"
		1.2829	1.69 ± 0.27	238 ± 5	"
GRB 210619B	1.937	0.1057	2.2 ± 0.7	22.0 ± 10.0	[19]
		0.1070	2.6 ± 0.8	2.0 ± 8.0	"

Notes. We include only the values from literature for which we calculate $P/\sigma_P > 3.0$ with T_{mid} in observer frame. (*) From the spectropolarimetric measurements in (Barth et al. 2003), since we do not consider chromaticity in the polarisation, we show the median value of the measured polarisation on the different wavelength bins, for the three epochs they presents. (**) For GRB 030329 we made use of the data presented in Covino & Gotz (2016) and, specifically, the results presented in this review taken from Greiner et al. (2003) and Magalhaes et al. (2003).
References for values from literature are: [1] (Covino et al. 1999), [2] (Wijers et al. 1999), [3] (Rol et al. 2000), [4] (Masetti et al. 2003), [5] (Bersier et al. 2003), [6] (Covino et al. 2003), [7] (Barth et al. 2003), [8] (Gorosabel et al. 2004), [9] (Rol et al. 2003), [10] (Covino & Gotz 2016), [11] (Gorosabel et al. 2010), [12] (Brivio et al. 2022), [13] (Steele et al. 2009), [14] (Uehara et al. 2012), [15] (Wiersema et al. 2012), [16] (Mundell et al. 2013), [17] (Wiersema et al. 2014), [18] (Urata et al. 2023), [19] (Mandarakas et al. 2023)